Project Luciole: A Wide-Field, High-Cadence Uncued Optical System For Comprehensive Tracking Of Decimeter-Sized LEO Objects

Denis Vida, Michael J. Mazur, Peter G. Brown, Stanimir Metchev,
David L. Clark, Tammy Do, Kuei Hung (Jack) Zhang
Department of Physics and Astronomy, University of Western Ontario, London, Ontario, Canada

Lauchie Scott
D*efence R&D Canada Ottawa, Ottawa, Ontario, Canada*

ABSTRACT

The recent proliferation of megaconstellations in low-Earth orbit (LEO) has led to a need for increased revisit frequency for purposes of space situational awareness (SSA) and environmental impacts. For example, the ability to remove mega-constellation satellite trails from astronomical imagery requires frequent Two-Line Element (TLE) updates, especially for objects with automatic electric propulsion and orbital control. Additionally, with large numbers of operational LEO objects, there is a greater requirement for assessment of spacecraft state of health and stability, which can be addressed, in part, through lightcurve measurements. To meet these goals, we have repurposed software and video cameras designed for faint meteor measurements as part of the Global Meteor Network while still allowing for meteor data collection. Our prototype system consists of 14 medium to narrow-field video cameras that cover the entire sky above 30 degrees elevation from a single site in a fly's eye configuration. Each camera has a field of view that covers roughly 100 sq deg of the sky. The system's limiting sensitivity for LEO objects is to optical magnitudes between +10 and +11, imaging at 25 Hz. The wide fields of view are well matched to the Canadian climate where partly cloudy conditions can frequently occur and the software allows for uncued tracking to continue in open clear spots in the sky. The concept of operations is of an all-sky viewing bubble in staring mode where all LEO objects larger than 30 cm crossing the bubble are captured. Initial observations from one prototype system yield in excess of 1500 satellite detections per night with ~1 million individual metric measurements per one 12-hour night. Satellites are tracked in a wide arc across the sky during their whole period of visibility. The narrow-field cameras have a plate scale of ~30 arcseconds per pixel, allowing for a total measurement accuracy of 5 arcseconds after centroiding and even less after applying a track-and-stack algorithm. Applying custom timing synchronization we have demonstrated millisecond-level timing accuracy. The satellite detection algorithm is a modified meteor-tracking algorithm which relies on detecting linear features in the imagery and registering objects which are consistent with roughly linear motion over time. The high astrometric accuracy is achieved by applying a novel astrometric method capable of accurately modeling distortions of wide-field lenses. The astrometric calibration is refined for each measurement, ensuring optimal measurement accuracy. Compared to other ground-based camera systems, the high cadence of our system enables accurate tracking of satellite light curves and the determination of their rotation states to an accuracy of ± 0.15 magnitude. Finally, our system is extremely low-cost, enabling wide distribution and little maintenance overhead due to simple design with no moving parts. In addition, the cameras can be adjusted to work in bright environments and during dusk and dawn, enabling tracking of re-entering objects. In this paper, we describe the methodology and first results from this system including calibration accuracy and photometric results of space objects overflying Canada. We describe how this class of sensors can be applied to detecting bright megaconstellation objects and describe the measured photometric appearance of constellation objects above Canada. As of mid-2024, the project is expanding to five sites across Canada, including one above the Arctic Circle. A public-facing webpage is soon to be available which will provide summaries of the detected positions and brightness for LEO objects in near real-time, data exploration, and allow the download of raw measurement data.

1. INTRODUCTION

Since the first launch of SpaceX Starlink satellites in late 2019, there has been an unprecedented increase in megaconstellation infrastructure in low-Earth orbit, with an order of magnitude more planned satellites to be launched in the next decade. This emerging paradigm shift presents novel space situational awareness challenges in terms of the capacity needed for timely catalog updates for spacecraft safety [1]. Individual object tracking using optical methods can be cost-prohibitive and slow due to the time necessary to acquire and then collect data in traditional

point-and-shoot methods. Radars are expensive and their geographical distribution is limited, making tracking low-altitude LEO objects with limited area of visibility challenging. This is particularly relevant for the most common type of Starlink satellites operating in the V-band (between 40 to 75 GHz), with over 12,000 planned for launch at heights in Very Low Earth Orbit (VLEO, between 330 – 350 km) which will have the smallest ground coverage for internet service. To complicate matters, these low-altitude satellites will suffer the most atmospheric drag and perform automated maneuvers making their orbital custody challenging. Due to their low elevation and relatively large cross-sectional area, megaconstellation satellites also tend to be relatively bright, often even visible to the naked eye. The total impact of these satellites on the night sky, astronomical observations, and animal behavior is not well understood due to the lack of widespread optical monitoring, but initial findings point to significant disruptions [2].

In this work, we present a novel concept for a ground-based optical system using extremely low-cost video cameras which represent a hybrid in capability between traditional optical and radar methods and are optimized for persistent megaconstellation observations. The camera design and software are based on meteor camera systems used by the Global Meteor Network [3]. Our Luciole cameras (French for "firefly"), enable uncued observations of all LEO objects larger than ~30 cm up to the altitude of 1000 km. The cameras are organized in a fly's-eye configuration (8 wide-field and 6 narrow-field cameras) covering the whole sky above an elevation of 30 degrees, affording coverage of the complete visible passages of over 2000 unique satellites per night from a single site at a cadence of 25 frames per second. As an example of the system's performance, Figure 1 shows a co-added image from a single camera showing the detected tracks of over 1000 satellites in a single night on May 31, 2024.

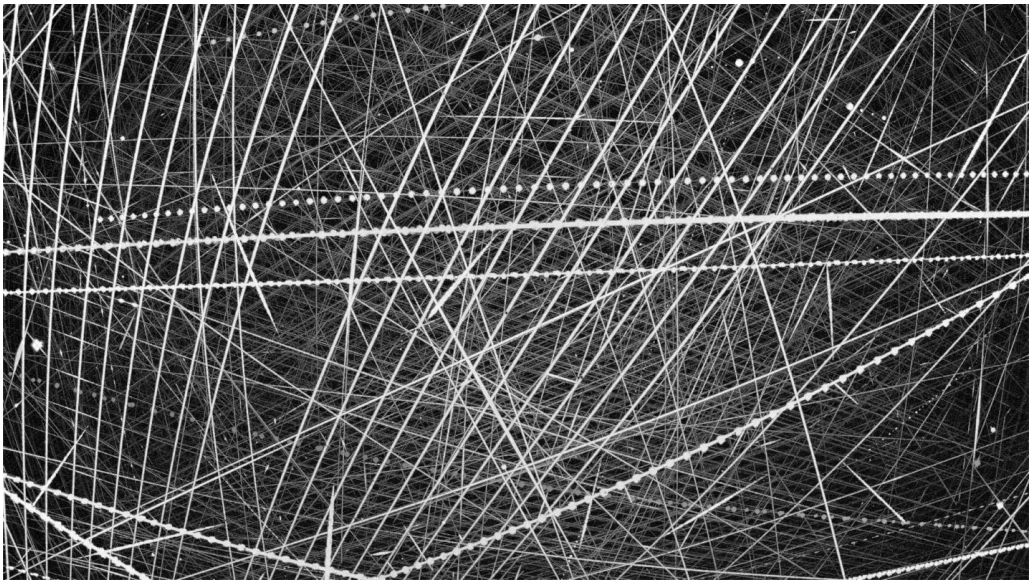

Fig. 1. Co-added image of all satellite detections on the night of May 31 - June 1, 2024 from a single camera. Objects appearing as dotted lines are aircraft strobes and are rejected by software. Also shown are meteor trails and trailed star images.

The first Luciole system was deployed at the beginning of 2024 in Southwestern Ontario, with one system deployed in the Arctic (above the extent of the Aurora) in August 2024 and more planned to be deployed across Western Canada in the fall of 2024.

In Sections 2 - 5 we describe the details of the hardware, in Section 6 we investigate the detectable populations of objects that can be observed with the systems, in Section 7 we discuss the software developed for satellite tracking, in Section 8 we simulate the orbital accuracy that can be achieved by using our systems, and in Section 9 we validate and evaluate the real-life observational performance of the systems and present some first results.

2. HARDWARE SOLUTION

Our hardware design uses commercial-off-the-shelf low-light security cameras equipped with Sony STARVIS2 sensors, the details of which are given in Table 1. The cameras are operated at 25 frames per second and with a resolution of 1920 × 1080 pixels (px). The cameras are arranged in two configurations: a dome with all-sky coverage above 30 deg of elevation and a fence (within the dome field of view) with more sensitive cameras covering a strip of the sky in a fence configuration. The dome system is composed of eight wide-field cameras, each using an 8 mm lens and giving a field of view of 57° × 30° with a plate scale of 1.6 arcmin/px. The fence is composed of six narrow-field cameras with 25 mm lenses with a field of view of 17° × 10° and a plate scale of 0.5 arcmin/px.

Table 1 – Hardware properties of the camera system. The limiting stellar magnitude (SNR = 3) is given for ideal conditions under dark skies.

	Num. cameras	Field of view	Plate scale	Astrometric accuracy	Stellar limiting magnitude
Wide-field	8	57° × 30°	1.6 arcmin/px	13 arcsec	+8
Narrow-field	6	17° × 10°	0.5 arcmin/px	5 arcsec	+10.5

Each array of cameras uses a dedicated high-end computer that performs real-time detection and calibration. Satellite correlation is done using the publicly available catalog from Space-Track.org, and the Skyfield[1] Python library.

The two camera sub-systems are deployed together, as shown in Figure 2.. The eight wide-field cameras are located in the center of the camera battery while the larger narrow-field cameras are placed at the edges. The short focal length and the robust construction of the wide-field 8 mm lenses enable them to stay in focus even during transport, while 25 mm lenses are equipped with custom-built focusers that enable remote focusing.

Fig. 2. A render of the Luciole camera system. Wide-field 8 mm cameras are in the middle while the narrow-field 25 mm cameras are at the edges of the battery.

[1] Skyfield library: https://rhodesmill.org/skyfield/ (accessed August 8, 2024)

3. WIDE FIELD SYSTEM CALIBRATION

The wide-field systems have been explicitly developed with the understanding that they will not directly achieve the industry-standard accuracy of better than 5 arcseconds on a single image, achieving only about ~13 arcseconds. However, in Section 8, we show that our wide-field systems can achieve an equivalent or better orbital accuracy than a standard Space Surveillance Network system with an accuracy of 1 arcsecond and a measurement cadence of one measurement every 6 seconds. The required orbital accuracy can be achieved by including measurements at a higher cadence of at least 5 per second. Another advantage of the high cadence of our systems is that all satellites remain point sources at satellite angular rates, not requiring them to be detected as streaks. Observations at 25 FPS can easily be combined to produce lower-cadence measurements at a higher level of astrometric accuracy.

Figure 3 shows the astrometric calibration on a wide-field camera using 66 calibration stars. The astrometric fit has been done using the radial distortion methods developed by [3], with atmospheric refraction taken into account. The root mean square of the astrometric fit is 12.6 arcseconds, showing no trends with any image axis or radially.

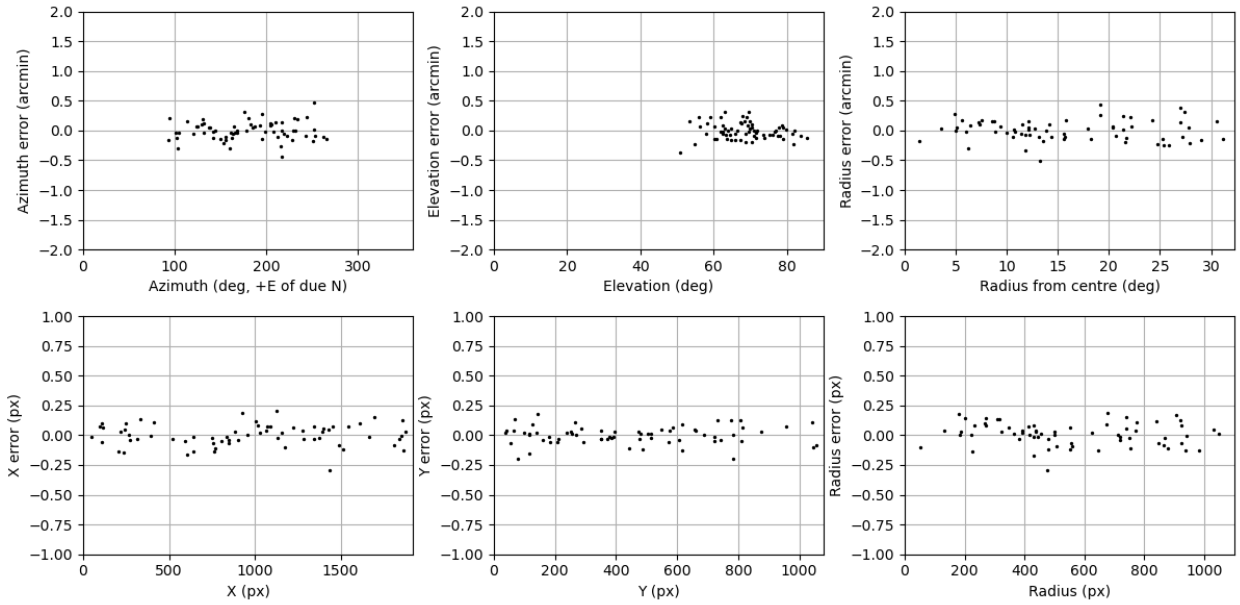

Fig. 3. Astrometric calibration on stars using a wide-field camera equipped with an 8 mm lens.

Figure 4 shows the stellar photometric calibration of an 8 mm camera with data recorded at a non-ideal site in Southwestern Ontario. The camera is operated with a gamma value of 0.45 to increase the dynamic range of the 8-bit sensor. The left inset shows the fit of instrumental magnitudes of stars (corrected for atmospheric extinction and vignetting) to their catalog values. The GAIA DR2 catalog was used and the photometric fit was done in the GAIA G photometric band which approximates the spectral response of our sensor [4]. The photometric fit error is ± 0.15 magnitudes, typical for our instruments. The upper right inset shows the effect of lens vignetting which is modeled using a $\cos^4$ radial drop-off from the optical axis. This approach is typically used for meteor cameras, as flat fields are difficult to create and maintain over a long period of time. Due to the short focal length, dust and other high-frequency variations in the sensitivity across the field of view are not visible. The sensor is ~1.5 mag less sensitive in the corners than in the center of the optical axis. Finally, the bottom right inset shows the effects of atmospheric extinction as estimated using the Green [5] model. At elevations > 30°, extinction is not important as is at most 0.3 mag in the bandpass of our sensors.

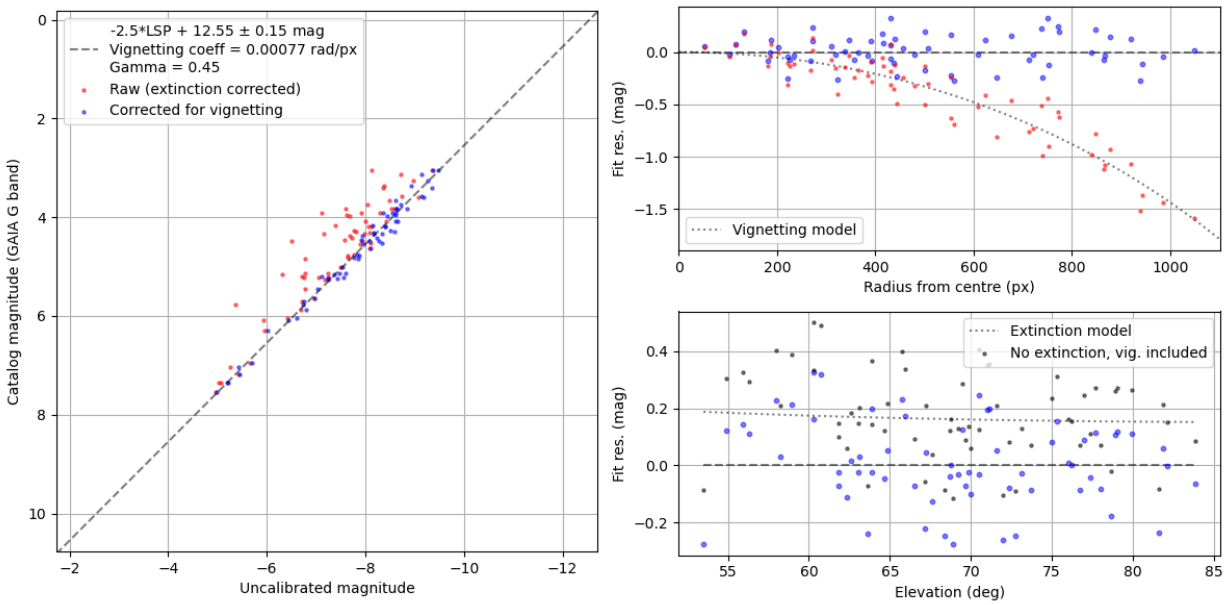

Fig. 4. Photometric calibration of a camera equipped with an 8 mm lens.

4. NARROW FIELD SYSTEM CALIBRATION

The narrow-field systems achieve a per image measurement accuracy of 4-5 arc seconds (~0.08 arcmin) due to the small plate scale and the high accuracy of the model used to model the lens distortion. Figure 5 shows the astrometric fit calibration errors of one camera with a 25 mm lens. A total of 77 stars were used in the fit, achieving root-mean-square fit residuals of 0.14 px pixels and 4.52 arc seconds, showing no trends.

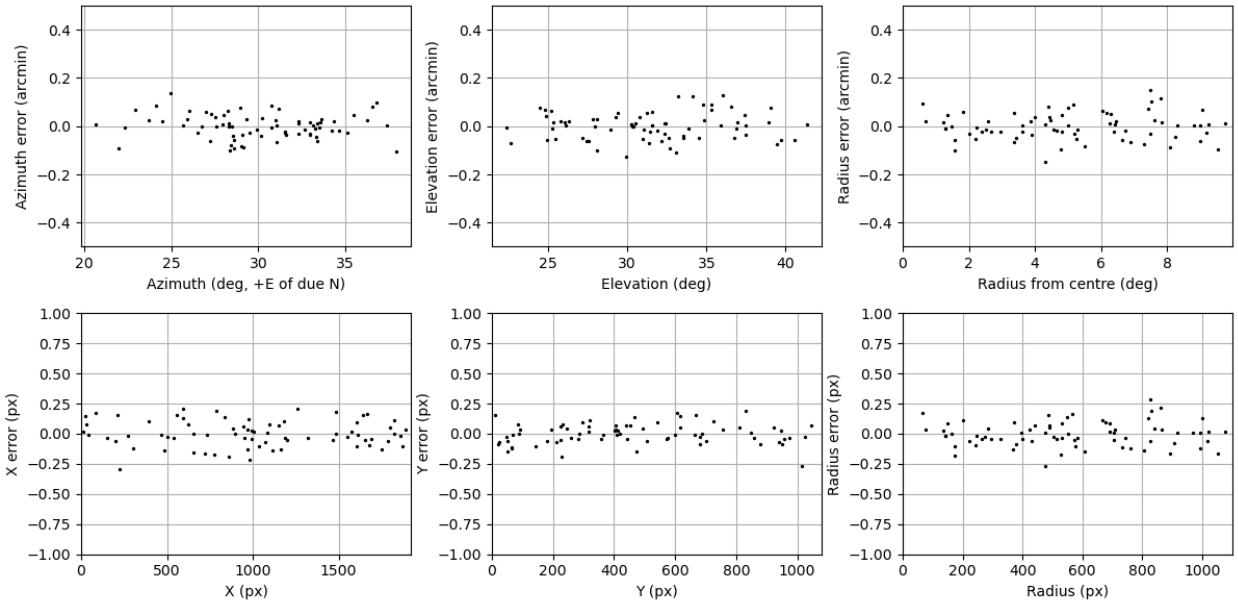

Fig. 5. Astrometric calibration of a camera equipped with a 25 mm lens.

Figure 6 shows the photometric calibration of the same camera. Unlike the 8 mm lens, the narrow-field 25 mm lens has significantly less vignetting and the sensitivity at the edges drops only 0.4 mag compared to the center. A photometric accuracy of ± 0.15 magnitudes is typical and not driven by the poor signal-to-noise ratio (> 10 for stars brighter than +8.5 mag) but by the spectral difference between the catalog bandpass and the bandpass of the sensor.

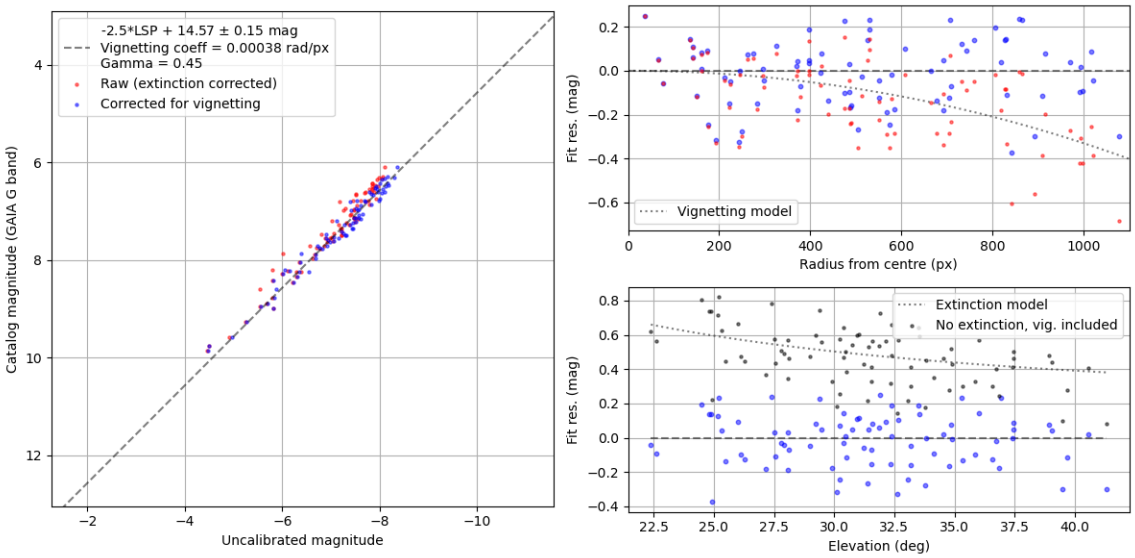

Fig. 6. Photometric calibration of a camera equipped with a 25 mm lens.

5. TIMING ACCURACY

Due to the requirement of high timing accuracy for satellite observations, we condition the clock of the computer running the cameras using a GPS device and the *chrony* software. Figure 7 shows the stability of the computer clock over a period of three days. The clock experiences a maximum deviation of only ~20 µs and most of the time it is accurate to less than 1 µs. Our data is not directly time-stamped at the sensor but at the arrival of the video frame to the buffer, the time of which is accurately tracked.

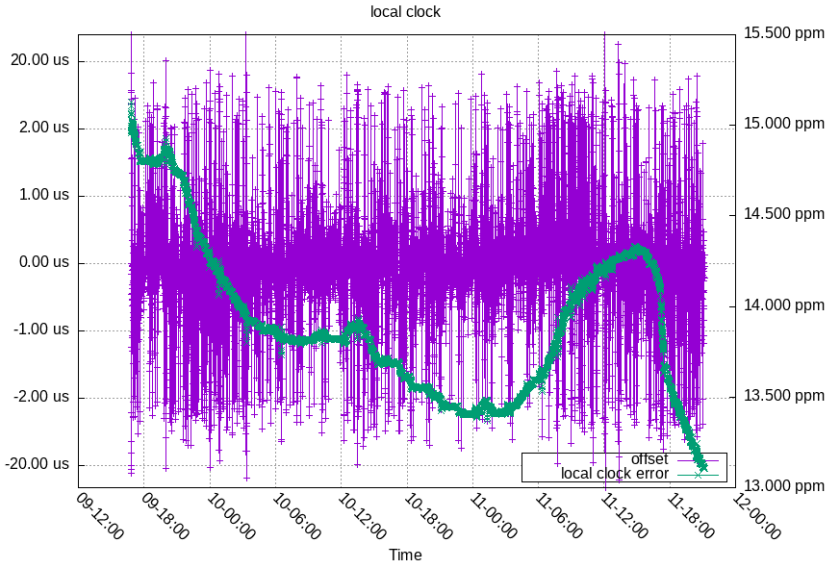

Fig. 7. Computer clock drift over a period of three days (August 9 -12, 2024).

The time of the arrival of the video frame to the buffer is accurately tracked, and the offset from the nominal expected time is shown in Figure 8. The top inset of the plot shows timing differences between a 256-frame block of frames, showing that there are no dropped video frames. The bottom inset shows timing differences between the blocks, showing that they are very steady and always less than 1 ms from the expected value, on average closer to 0.1 ms. This plot shows that the relative time between frame collection and arrival to the video buffer is much less than an interframe time.

The two top plots in Figure 8 show the accuracy of the absolute clock time and the relative time between video frames. However, there is one other potential source of timing error – th absolute time difference between frame collection and arrival to the video buffer. This final absolute time difference is on the order of 50 ms and does not change over time or from camera to camera. This value is applied as a fixed time correction to the observations. The value was confirmed using a laboratory setup where the absolute camera time was directly measured and validated using calibration satellites. For data validation, a special timing camera is also installed with each system to monitor any potential changes in the absolute time offset. This timing camera observes regular flashes produced by a device governed by a GPS-synchronized instrument.

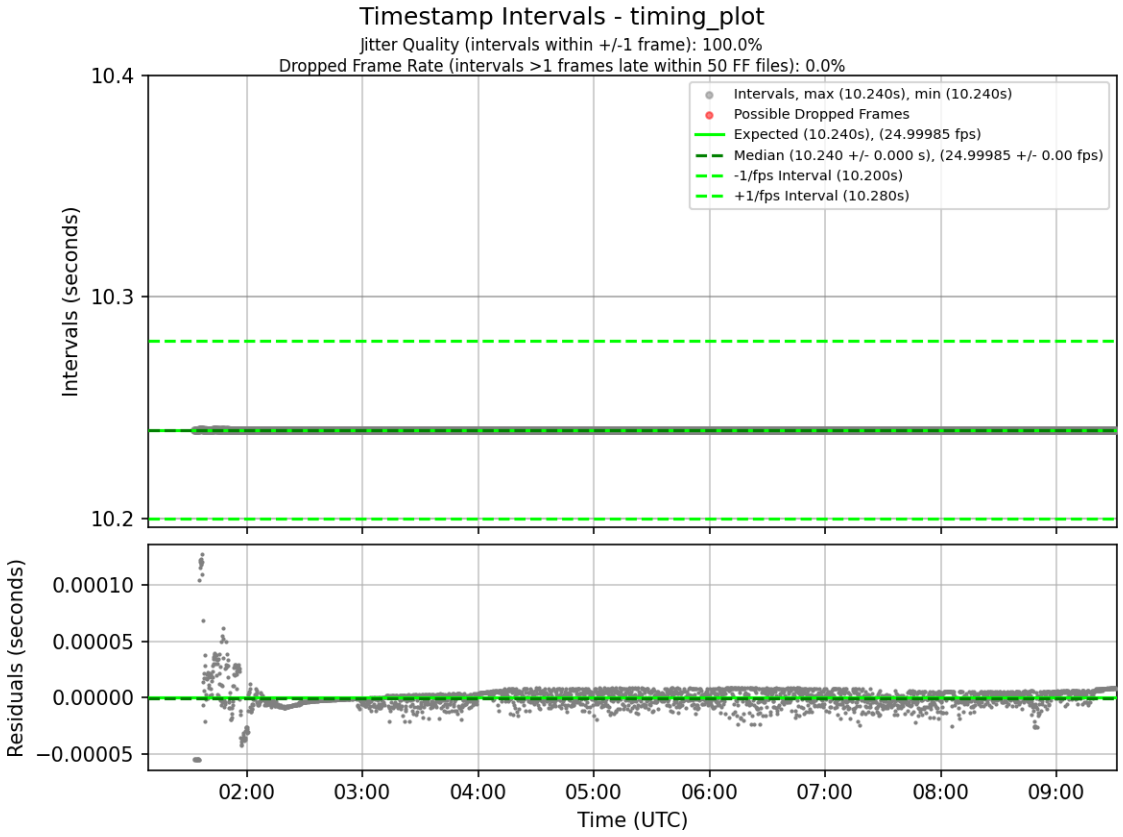

Fig. 8. Intervals between 256-frame video chunks, stable at the expected time. Bottom: Timing errors from the expected time.

6. DETECTABLE POPULATIONS

Figure 9 shows the density map of satellite altitudes and radar cross-sections (RCS) available in the CelesTrak catalog[2] up to 4000 km. Overlaid on top are curves showing the diameters of objects at the limiting sensitivity of the two camera systems (blue for the dome cameras, red for the fence). Additional curves for object reflectivity of 10% (debris) and 20% (operational objects) are shown for each camera group [10].

The cross-sectional area A (which we use as a proxy for RCS) is computed using the following magnitude equation

$$m_v = -2.5 \log_{10}(A \cdot \rho \cdot \theta) + 5 \log_{10}(r) - 26.7 \quad (1)$$

where m_v is the magnitude of the satellite, ρ is the reflectivity (dimensionless), Θ is the phase angle coefficient (assumed $\Theta = 0.08$ for a specular sphere), and r is the distance to the satellite in meters [11]. The value of -26.7 is the zero point in the visual bandpass and is the apparent magnitude of the Sun at Earth.

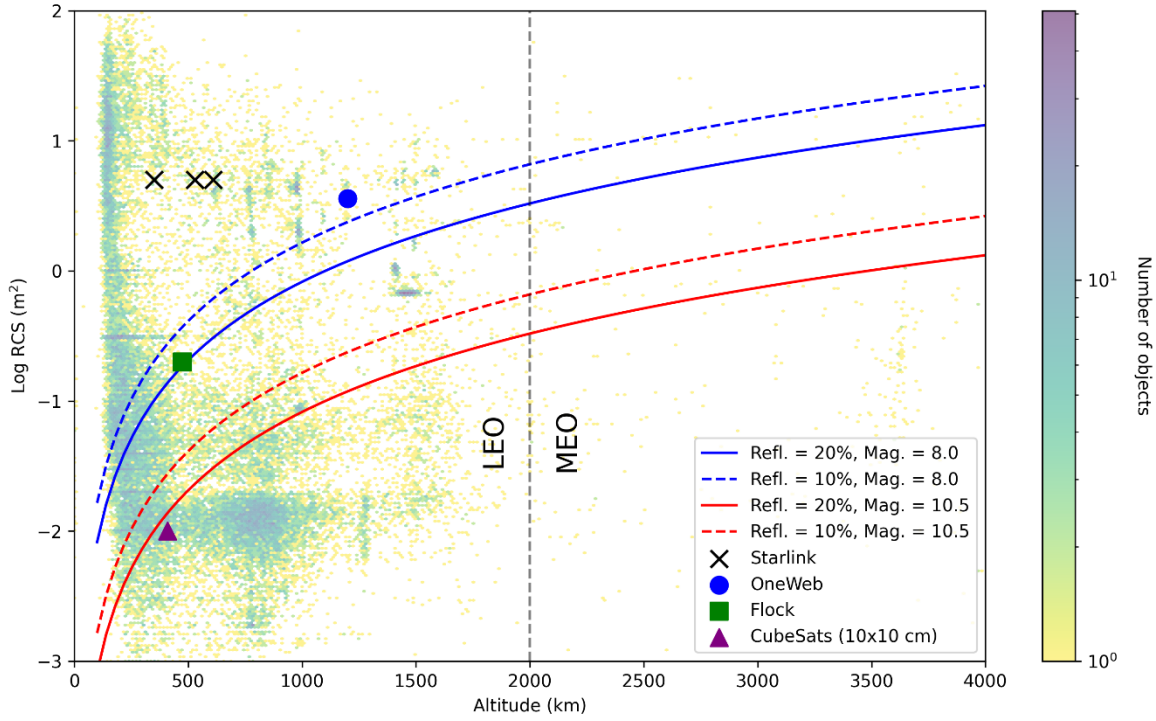

Fig. 9. Satellite populations observable by the systems (data from CelesTrak). The blue curves represent the wide-field and the red curves the narrow-field camera sub-systems. Solid curves are computed with a reflectivity of 20% (appropriate for satellites) and dashed curves with a reflectivity of 10% (debris). Objects above the curves are theoretically detectable by the sensors.

The wide-field cameras can observe all megaconstellation satellites (Starlink and OneWeb), as well as smaller constellations such as Flock [8]. We expect that future megaconstellations (e.g. the Guowang, Thousand Sails) will have similar physical parameters and will be observable. At an altitude of 1000 km, the limits of the wide-field system are around RCS of 1 m^2, and around 0.05 m^2 at the lowest useable orbital altitude.

The narrow-field cameras push to about an order of magnitude lower RCS values, observing 0.1 m^2 objects at 1000 km and almost being able to observe 10x10 cm CubeSats launched from the ISS. Due to our conservative phase angle

[2] CelesTrak satellite catalog: https://celestrak.org/satcat/search.php (accessed July 17, 2024)

assumptions, some even smaller objects could be observed at more favorable phase angles. Luciole sensitivity is just outside of the range of debris in the 700 – 1000 km range, but some of these could be observed with targeted cameras with an increased sensitivity.

7. SOFTWARE

The capture, detection, and calibration software is an adaptation of the validated software library used by the Global Meteor Network [3] developed for meteor observations. This software as modified allows for automated uncued and multi-target tracking of satellites, effectively detecting all moving sources inside the field of view of a camera down to a specified noise threshold.

The software automatically plans observation periods based on the position of the Sun and performs the data collection. During the detection procedure, the individual video frames are thresholded using a signal-to-noise ratio of ~3 and candidate detections are verified by postulating a near-linear propagation of the object in the image plane and in time. An additional localization filtering step is applied which tightly separates the object from the background. In the final detection step, the position and the brightness of the object is measured. To ensure the data quality, an automated recalibration step is performed which refines the camera pointing (which may drift due to thermal effects) and performs a photometric calibration for each track.

Once a day, a satellite catalog is downloaded from Space-Track.org and passages are predicted for the location of the sensor using the Skyfield software library. Only those passages predicted to be sunlit and visible in the field of view of the sensor are kept. Once data is available, the tracks are correlated with objects in the catalog using Skyfield. Only detections with at least six points and slower than 2 degrees per second are selected for correlation, as faster-moving detections are most often meteors (which are saved for analysis in a separate pipeline). A correlation is considered successful if it falls within the predicted time interval of the passage and its direction of motion and location are within pre-set thresholds. In the final step, the measurements correlated to satellites are reported in a custom CSV format which is sent to the customer.

8. MODELLED ORBITAL ACCURACY DERIVED FROM LUCIOLE MEASUREMENTS

We developed an orbit optimization algorithm implemented in Python that takes a satellite's two-line element, TLE, and attempts to correct the orbital elements contained in the TLE using observations to provide an updated TLE with a static epoch. It does this by minimizing an objective function that returns a scaled root mean square deviation (RMSD) between the predicted and observed right ascension and declination (RADEC) coordinates for an observer with a known position. We use SGP4 (available in Skyfield) to produce numerical propagations of satellite positions based on hypothesized orbital elements. Our optimizer uses the Nelder-Mead algorithm to vary orbital parameters and produce the best fit on synthetic observations simulated to reproduce Luciole measurements. The individual orbital parameters are passed as parameters rather than the TLE because the precision in a TLE is limited to 4 or 7 decimal places for the parameters and the optimizer that is called the objective function is expecting a differentiable function. The objective function would have jump discontinuities if the optimizer needed to guess TLEs rather than the individual orbital parameters.

To test the optimizer with synthetic data, a Python script was implemented to generate RADEC values by propagating a TLE to predicted passage times, sampling at the cadence of the simulated sensors, and adding noise to the propagated values to simulate the measurement errors in the camera systems. Several simulations have been made to guide the design of the Luciole cameras and demonstrate the theoretical capabilities of Luciole compared to the existing observatories used by the Space Surveillance Network (SSN).

Table 2 lists the simulated systems, their hypothesized accuracy, and the cadence at which they produce data. The current instruments that contribute to the SSN have been simulated with a 1 arc second accuracy and a cadence of one measurement every six seconds, and with the assumption that the full passage from a ground site has been captured. The Luciole wide-field cameras were simulated assuming the complete visible passage of the satellite has been captured with an accuracy of 13 arc seconds and a cadence of 25 frames per second. The accuracy of narrow-field cameras has been assumed to be 5 arc seconds, but two different configurations have been assumed: The current fence configuration which can only capture a short 10° arc (worst case); A hypothetical ring configuration where 25 mm

lens camera cover a ring in the sky at an elevation of 30° capturing two segments of the passage in separate times to maximize the total observed arc. Finally, a Global Meteor Network camera designed for observing meteors has also been simulated, assuming a measurement accuracy of 60 arc seconds and that it captures a complete satellite passage across the entire sky.

Table 2 – Simulated Systems

System	Accuracy (Arc Seconds)	Cadence (Frames Per Second)	Field of View
SSN	1	⅙	Full Sky
Luciole wide-field	13	25	Full Sky
Luciole narrow-field	5	25	10° arc or Ring
GMN meteor camera	60	25	Full Sky

Table 3 – Model-examined satellites and the passages used for the simulation

Satellite	Passage Start (UTC)	Passage Apex (UTC)	Passage End (UTC)
Blue Walker 3	Aug. 1, 2024 09:05:44	Aug. 1, 2024 09:07:50	Aug 1, 2024 09:09:58
COSMOS 2344	Aug. 1, 2024 04:30:06	Aug. 1, 2024 04:31:28	Aug. 1, 2024 04:38:41
Helios 1B	July 30, 2024 03:08:57	July 30, 2024 03:13:15	July 30, 2024 03:15:08
Sea Sat 1	July 10, 2024 04:32:25	July 10, 2024 04:33:10	July 30, 2024 04:38:08
Tiangong	July 30, 2024 01:31:30	July 30, 2024 01:34:34	July 30, 2024 01:37:38
ISS	Aug. 19, 2024 09:29:33	Aug. 19, 2024 09:31:52	Aug. 19, 2024 09:34:11

The satellites considered in the simulation are given in Table 3. The camera systems with full sky coverage are simulated to observe the satellites from start to finish of the full passage, while the narrow-field camera is simulated to observe the satellite 17 seconds before and after the passage apex (approx. 10° on average), where the satellite is highest in the night sky.

The TLEs were retrieved from the N2YO website[3]. The perturbed orbital parameters used in the simulation were derived by increasing the mean anomaly *M* such that the satellite is one second early and increasing the inclination *i* by the arcsin of the reciprocal of the mean anomaly, essentially moving the satellite 1 km to the side. The formulas for both perturbations are:

$$M_{new} = M_{old} + \frac{n}{240} \tag{2}$$

$$i_{new} = i_{old} + \frac{180}{\pi} arcsin\left(\frac{1000}{a}\right) \tag{3}$$

[3] N2YO website: https://www.n2yo.com/ (accessed August 15, 2024).

where M is the mean anomaly (degrees), n is the mean motion (revolutions per day), i is the inclination, and a is the semi-major axis (meters). The semi-major axis can be derived using

$$a = \left(\frac{\mu}{\omega^2}\right)^{\frac{1}{3}} \quad \mu = 3.986004418 \times 10^{14} \text{ and } \omega = \frac{2\pi n}{86400} \tag{4}$$

where μ is the gravitational parameter for Earth in units of meters cubed per second squared and ω is the satellite's angular velocity about the center of the Earth. Table 4 contains the investigated TLEs and perturbed orbital elements for each satellite.

Table 4 – Reference TLEs of simulated satellites and the values of the perturbed inclination and mean anomaly.

Satellite	TLE	Perturbed Inclination (Degrees)	Perturbed Mean Anomaly (Degrees)
Blue Walker 3	1 10967U 78064A 24192.94248397 .00000479 00000-0 17609-3 0 9998 2 10967 107.9981 293.5685 0002478 279.5026 80.5839 14.45014314418823	53.2454482445	136.455220974
COSMOS 2344	1 24827U 97028A 24213.56799649 .00000017 00000-0 70509-3 0 9998 2 24827 63.3103 275.8611 1074319 60.7516 34.2112 11.07973184 98721	63.3170412478	34.2573655493
Helios 1B	1 25977U 99064A 24211.36736898 .00001673 00000-0 20518-3 0 9994 2 25977 98.2392 84.4221 0001895 127.8358 232.3027 14.84550974597875	98.2473931493	232.364556291
Sea Sat 1	1 10967U 78064A 24192.94248397 .00000479 00000-0 17609-3 0 9998 2 10967 107.9981 293.5685 0002478 279.5026 80.5839 14.45014314418823	108.006147029	80.6441089298
Tiangong	1 48274U 21035A 24211.21968604 .00016374 00000-0 20687-3 0 9999 2 48274 41.4677 186.6257 0001649 314.2592 45.8111 15.59175156185679	41.4761654633	45.8760656315
ISS	1 25544U 98067A 24226.93337752 .00035269 00000-0 62105-3 0 9997 2 25544 51.6419 29.2513 0005296 199.2132 296.7788 15.50087060467500	51.6503325357	296.843386961

The optimized TLEs were then used to propagate the satellite's position from the start of the visible pass to 100 minutes into the future, corresponding to about one full orbit. These propagated positions were compared with those from the original true TLEs. The total RMSD over one orbit and the displacement along the direction of motion and laterally from the direction of motion for each propagated position were calculated. All simulations were repeated 10 times with resampled noise, and the results were averaged for each combination of systems and cadence assumptions to smooth over the influence of noise sampling.

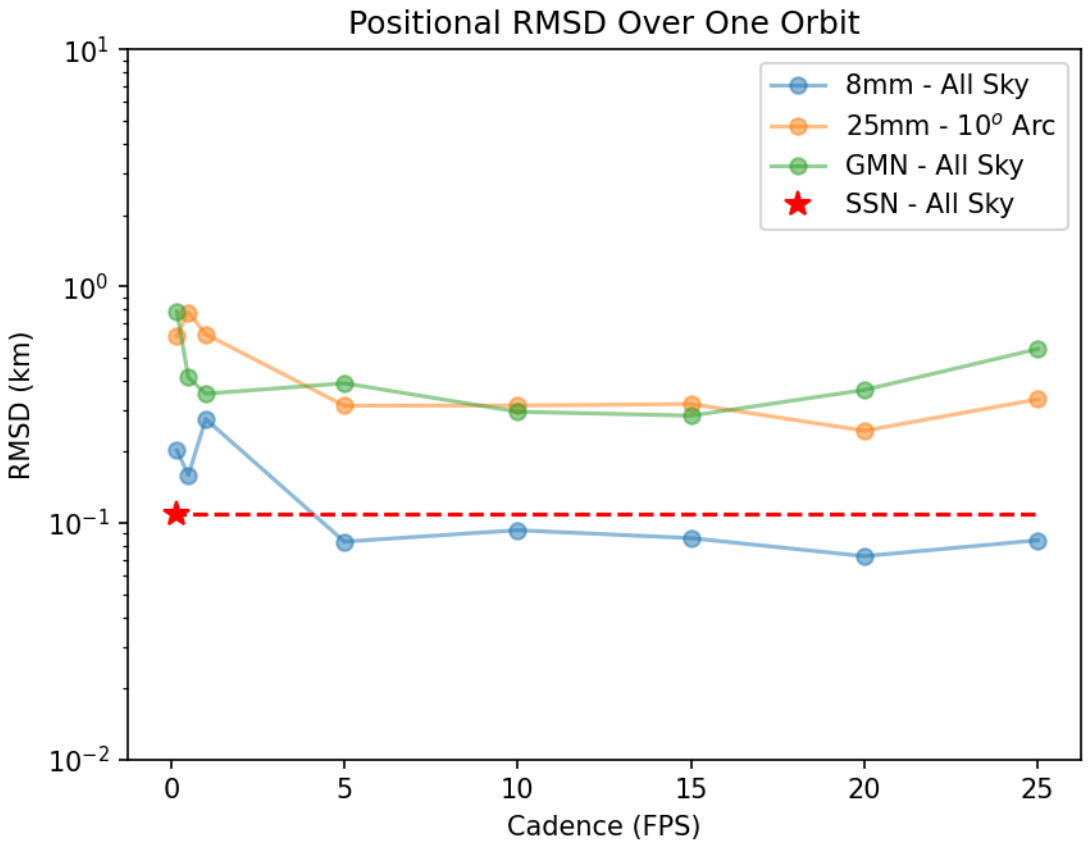

Fig. 10. Example of the displacement from the reference TLE for the Tiangong simulation.

Figure 10 shows the total positional error from the reference TLE for each simulated system and cadence. After the initial round of simulations was performed, we noted that the optimized TLEs from the simulated SSN observations resulted in very low errors even with a low cadence. The simulated wide-field systems fell well short of this performance when using the same cadence, but rapidly caught up when their cadences increased to 5 FPS from 1/6 FPS. Much less accurate GMN cameras do not achieve the same performance at any cadence. Surprisingly, the narrow-field 25 mm camera in the fence configuration do not achieve a good accuracy even with an FPS of 25. Because of its narrow field of view, even when a large sample of observations is generated, the optimized TLEs produced tend to have much greater errors than those generated by the other systems, even the less accurate cameras running at lower cadences. We strongly suspected that the reason is the very short observation arc of only 10°.

To investigate the full impact of observable arc length and to guide the camera design and pointing patterns, a further round of simulations was made using a ring of narrow-field cameras pointed to elevations of 30° and a hypothetical (but hard to implement in practice) system of narrow-field cameras covering the whole sky. The ring of 25 mm cameras captures the satellite in two short 10° arcs, once upon rising above the horizon, and once more before setting. Figure 11 shows the results of the additional simulations which show that the ring and all-sky configuration could match the performance of the other camera systems at cadences of greater than 1 frame per second while the single 25mm camera fell short. Similar behavior was found for all other investigated satellites.

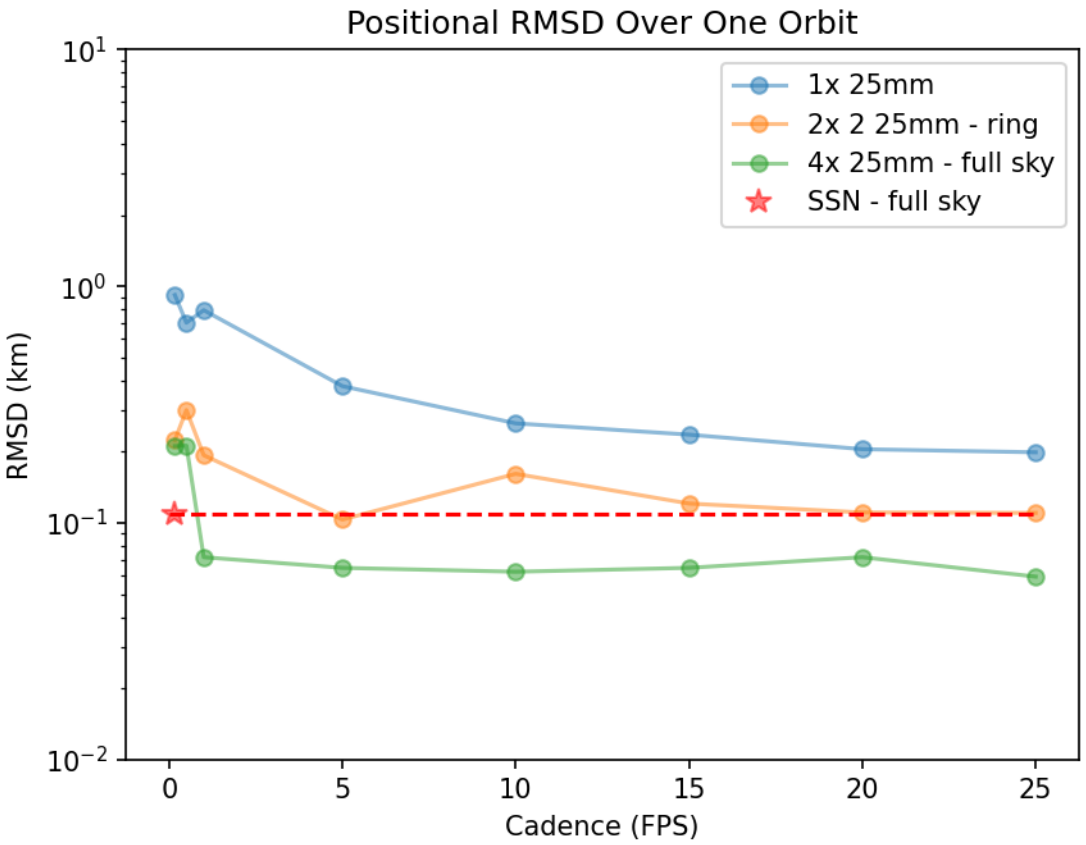

Fig. 11. Additional simulations with three configurations of narrow-field camera pointing for the Tiangong simulation

In conclusion, the simulations demonstrated that the enhanced cadence and field of view of the Luciole cameras drastically improve orbital element estimations, potentially outperforming existing systems in the SSN in terms of accuracy and temporal resolution. Specifically, our simulations underscore the importance of camera configuration and observation arc length in achieving optimal orbital predictions. The ring of narrow-field cameras and an all-sky done of wide-field cameras show the potential to match or surpass the performance of SSN sensors by effectively utilizing high cadence observations. However, orbit optimization methods will need to be able to ingest the high-cadence data produced by our cameras, potentially requiring changes in operational software.

9. INITIAL CAMERA RESULTS AND PERFORMANCE EVALUATION

A prototype wide-field system with 8 mm lenses has been in operation in Southwestern Ontario since the beginning of 2024. On an average clear night, each camera system observes ~1500 unique space objects, with a total of over 1 million individual measurements. Since the beginning of operation, a total of 13,207 unique objects from the public catalog have been observed with at least 6 measurements per track. Figure 12 shows the histogram of detected object brightness from a sample evening collected by the prototype wide-field sensor on 6 April 2024 using early photometric software. The sensor detects a limiting magnitude of 8 and shows a modal value near magnitude 6.25, though these are likely upper limits as the photometry pipeline at this stage was overpredicting magnitudes (reported brighter than they really are). Figure 13 shows the detected apparent magnitude vs the phase angle of the observation.

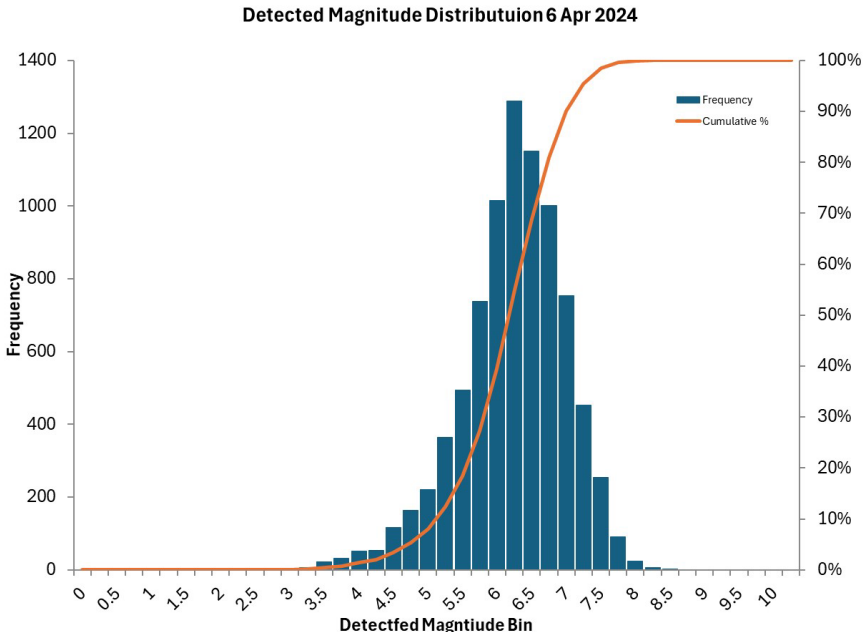

Fig. 12. Histogram of object brightness detected by the prototype wide-field camera system located in Southwestern Ontario on the night of April 6, 2024.

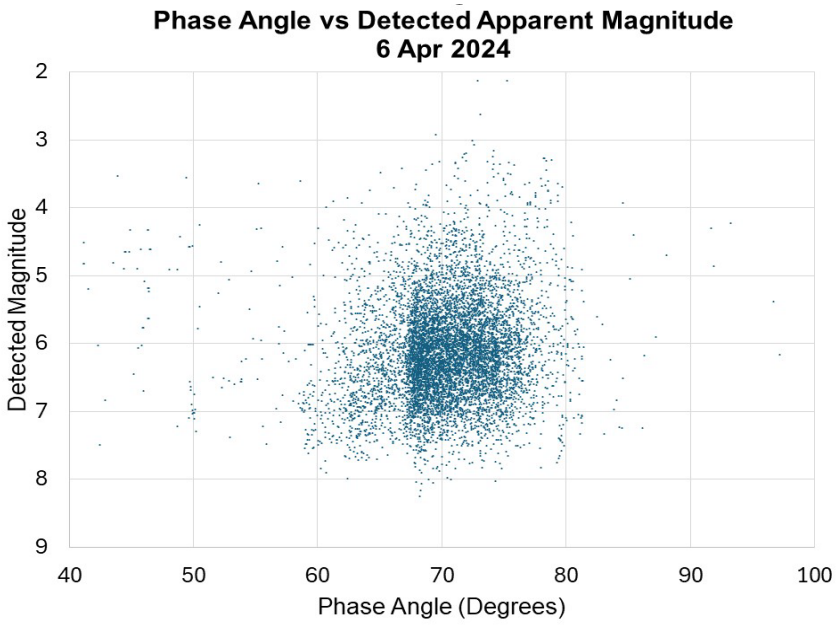

Fig. 13. The detected magnitude as a function of the Phase Angle from the wide-field sensor on April 6, 2024.

Fig. 14. shows the magnitude measurements of Cryosat 2 observed on July 13, 2024 at the full cadence of the sensor (25 frames per second). The scatter in the measurements is within the expected 0.15 mag error. The system allows satellite brightness to be tracked at all phase angles, helping to model satellite brightness and find optical pointing locations for astronomical observations to minimize megaconstellation impact.

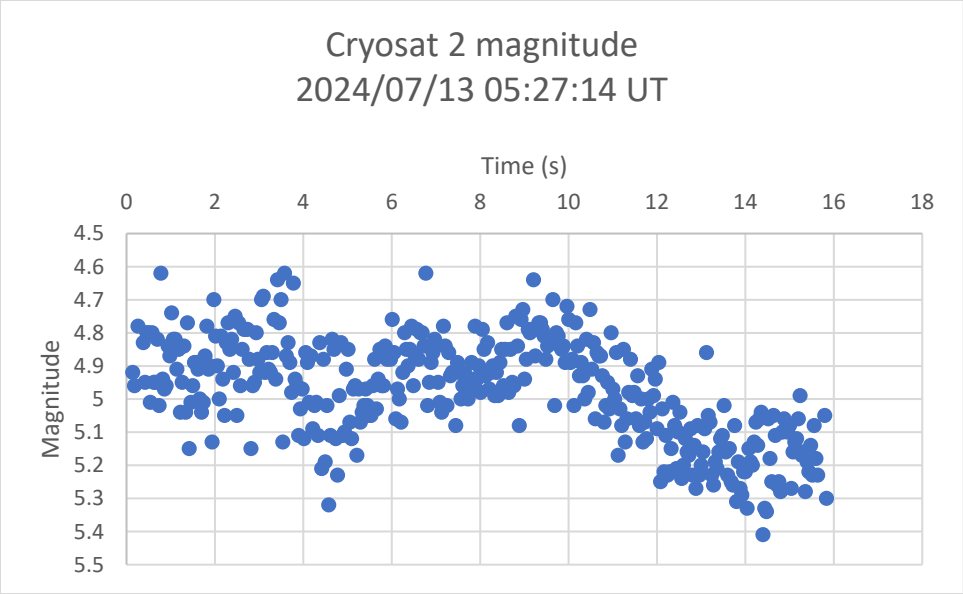

Fig 14. Measured magnitude of Cryosat-2 on July 13, 2024 at 25 fps.

The timing accuracy of the system has been confirmed by comparing the predicted positions of two calibration satellites, EGS (Ajisai) and Cryosat 2, with measured positions. The timing offsets were within the expected limits. The same procedure was repeated for all observed satellites and we found significant offsets from the catalog of up to 2 seconds (Fig. 15), showing that public TLEs of most observed satellites significantly differ from their actual positions, requiring daily observation.

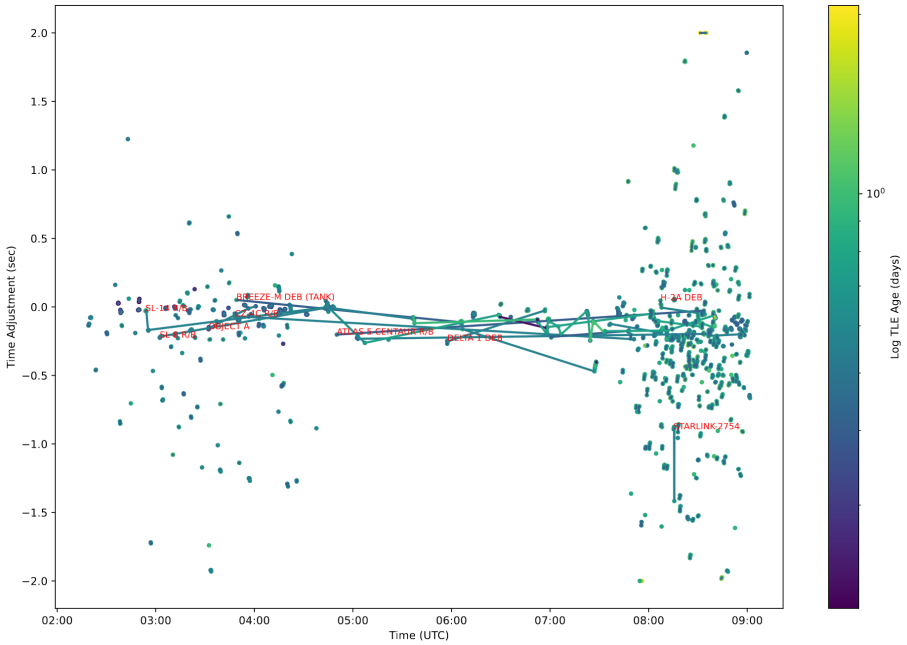

Fig. 15. Time offsets for observed satellites from a single narrow-field 25 mm camera on the night of July 19-20, 2024 as a function of the age of the used TLE (in days) shown by the color bar.

As of August, 2024, the astrometric accuracy of the system is in the process of evaluation. The point-to-point measurement precision is in line with expectations from the calibration and is very high compared to the precision written in SSN non-traditional sensor requirements [6]. The full astrometric accuracy evaluation of the system will be published at a later date.

Figure 16 shows the ground tracks of satellites observed by the two systems on a single clear night (July 20/21) with a total observing period of 7 hours. The wide-field system observed 1270 unique satellites with 7 operational cameras while the narrow-field system observed 1458 unique satellites with 6 cameras.

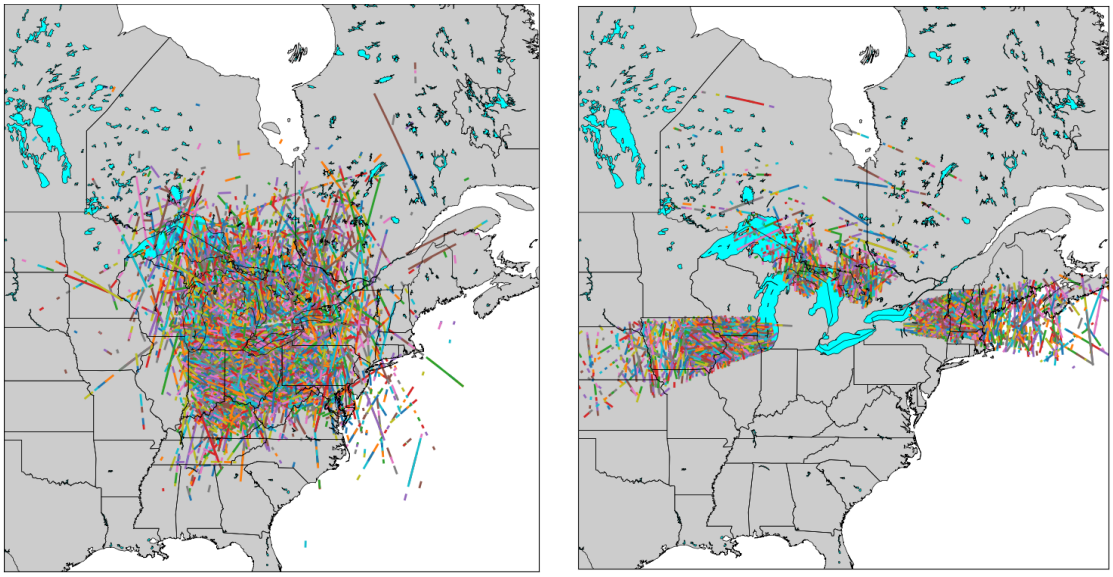

Fig. 16. Ground tracks of satellites observed by all cameras in a single night of July 20-21, 2024. Left: Wide-field system. Right: Narrow-field system.

Figure 17 shows the relative frequency of main satellite designations (>1% per system) observed by the two systems. Starlink dominates the observations by far, constituting about half of all observations. It is followed by rocket bodies and satellites operated by Russia and China. Other constellation satellites are also observed (Gaofen, Meteor, Globalstar, OneWeb, Iridium). Satellites not present in the catalog are also monitored and they constitute about a quarter of all tracks.

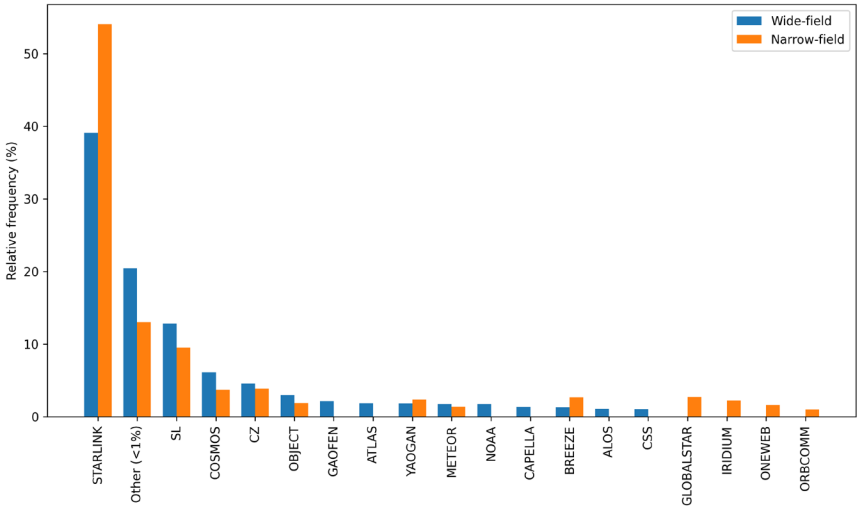

Fig. 17. Relative frequency of satellite designations observed by the two systems on July 20-21.

10. CONCLUSION

Our findings underscore the promising potential of adapting cameras optimized for detection of faint meteors for extensive tracking and characterization of space objects, particularly in the low Earth orbit (LEO) region being complementary to similar work done by the FireOpal project which arose from the Desert Fireball Network program [9] optimized for fireball recording. The system's high cadence and wide field of view enable precise measurements of the trajectories and rotational states of space objects, which are critical for updating satellite catalogues and assessing collision risks. These capabilities are particularly pertinent given the increasing density of orbital objects due to the expansion of satellite megaconstellations.

The systems will also have an additional purpose of measuring the flux of meteor showers by running the Global Meteor Network software [7]. The narrow-field cameras in particular will track the population of faint meteors which are rarely observed.

Moreover, the integration of narrow-field cameras specifically enhances our ability to observe smaller and fainter objects that are typically challenging to detect. This sensitivity is crucial for advancing our understanding of the spatial distribution and behavioral dynamics of smaller debris, which pose collision risks to operational satellites and spacecraft. The low cost, flexibility, and scalability of the Luciole system, evidenced by its deployment across multiple sites in Canada, including in challenging environments like the Arctic, highlight its adaptability and the potential for broader international application. The project's progression towards providing near real-time data access via a public-facing website will further democratize space situational awareness, allowing for wider participation in monitoring efforts and potentially fostering collaborative approaches to tackling space debris challenges.

In conclusion, Project Luciole represents a significant step forward in the utilization of ground-based optical systems for space surveillance and environmental monitoring. Its innovative approach not only enhances the accuracy and efficiency of space object tracking but also contributes to the broader field of astronomical observations by minimizing the interference caused by satellite trails. As the system continues to expand and evolve, it promises to play a pivotal role in the global efforts to ensure the long-term sustainability of space activities, facilitating a safer and more predictable LEO environment.

11. ACKNOWLEDGEMENTS

The authors would like to acknowledge the Canadian Department of National Defence ADM(DRDC) and the National Sciences and Engineering Research Council of Canada for their support of this work. Funding for this work was provided by the NASA Meteoroid Environment Office under cooperative agreements 80NSSC21M0073 and 80NSSC24M0060.

12. REFERENCES

[1] Zhang, J., Cai, Y., Xue, C., Xue, Z. and Cai, H., 2022. LEO mega constellations: review of development, impact, surveillance, and governance. *Space: Science & Technology*.

[2] Nandakumar, S., Eggl, S., Tregloan-Reed, J., Adam, C., Anderson-Baldwin, J., Bannister, M.T., Battle, A., Benkhaldoun, Z., Campbell, T., Colque, J.P. and Damke, G., 2023. The high optical brightness of the BlueWalker 3 satellite. *Nature*, *623*(7989), pp.938-941.

[3] Vida, D., Šegon, D., Gural, P.S., Brown, P.G., McIntyre, M.J., Dijkema, T.J., Pavletić, L., Kukić, P., Mazur, M.J., Eschman, P. and Roggemans, P., 2021. The global meteor network–methodology and first results. *Monthly Notices of the Royal Astronomical Society*, *506*(4), pp.5046-5074.

[4] Gaia Collaboration, 2018. VizieR online data catalog: Gaia DR2 (gaia collaboration, 2018). VizieR Online Data Catalog, pp.I-345.Space Based Space Surveillance (SBSS), eoportal.org, https://www.eoportal.org/satellite-missions/sbss, accessed 17 Aug 2023.
[5] Green, D.W., 1992. Magnitude corrections for atmospheric extinction. International Comet Quarterly, 14, p.55.
[6] Payne, T., Space Situational Awareness Metric Data Integration Guidelines for Non-Traditional Sensors, Air Force Space Command Instruction 10-610, HQ Air Force Space Command A3/6Z, 3 July 2019.
[7] Vida, D., Blaauw Erskine, R.C., Brown, P.G., Kambulow, J., Campbell-Brown, M. and Mazur, M.J., 2022. Computing optical meteor flux using global meteor network data. *Monthly Notices of the Royal Astronomical Society*, *515*(2), pp.2322-2339.
[8] Johnson, C., Scott, L. and Thorsteinson, S., 2021. Comparing Photometric Behavior of LEO Constellations to SpaceX Starlink using a space-based optical sensor. In *AMOS Conference*.
[9] Jansen-Sturgeon, T., Hartig, B., Bland, P., Madsen, G., Bold, M., Howie, R., Mason, J., Drury, R. and McCormack, D., 2018, September. FireOPAL: Continental-scale Coordinated Observations of the OSIRIS-REx Flyby. In *The Advanced Maui Optical and Space Surveillance Technologies Conference* (p. 45)
[10] Tyson, J.A., Snyder, A., Polin, D., Rawls, M.L. and Ivezić, Ž., 2024. Expected Impact of Glints from Space Debris in the LSST. *The Astrophysical Journal Letters*, *966*(2), p.L38.
[11] Williams, J.G. and McCue, G.A., 1966. An analysis of satellite optical characteristics data. *Planetary and Space Science*, *14*(9), pp.839-847.

SUMMARY OF PRESENTATION

We present a novel system based on video cameras with an all-sky coverage in a fly's eye configuration that can capture all overflying objects in LEO larger than 30 cm at a cadence of 25 Hz, with a sub-10 cm lower limit at lower altitudes and favorable phase angles. The system is primarily designed to monitor the fastest-growing LEO population – megaconstellations. The system provides positional and timing measurements during the complete visible flyover, as well as photometry which can be used to monitor satellite rotation states. Observations are not targeted but opportunistic, meaning that new objects can readily be captured and objects with uncertain orbits can be tracked. In addition, the low cost of the systems enables widespread deployment and monitoring of reentries. The main goal of the project is to provide the measurements openly on a public-facing website to foster a secure, safe, and sustainable space environment and provide a common dataset to the SSA community.